

Mass-Metallicity Relation from Cosmological Hydrodynamical Simulations and X-ray Observations of Galaxy Groups and Clusters

N. Truong^{1*}, E. Rasia^{2,3}, V. Biffi^{2,4}, F. Mernier^{1,8,9}, N. Werner¹, M. Gaspari^{5†},
S. Borgani^{2,4,6}, S. Planelles⁷, D. Fabjan^{10,2}, and G. Murante²

¹ MTA-Eötvös University Lendület Hot Universe Research Group, Pázmány Péter sétány 1/A, Budapest, 1117, Hungary

² INAF, Osservatorio Astronomico di Trieste, via Tiepolo 11, I-34131, Trieste, Italy

³ Department of Physics, University of Michigan, 450 Church St., Ann Arbor, MI 48109

⁴ Dipartimento di Fisica dell' Università di Trieste, Sezione di Astronomia, via Tiepolo 11, I-34131 Trieste, Italy

⁵ Department of Astrophysical Sciences, Princeton University, 4 Ivy Ln, Princeton, NJ 08544-1001, USA

⁶ INFN, Istituto Nazionale di Fisica Nucleare, Trieste, Italy

⁷ Departamento de Astronomía y Astrofísica, Universidad de Valencia, c/Dr. Moliner, 50, 46100 Burjassot, Valencia, Spain

⁸ Institute of Physics, Eötvös University, Pázmány P. s. 1/A, Budapest, 1117, Hungary

⁹ SRON Netherlands Institute for Space Research, Sorbonnelaan 2, 3584 CA Utrecht, The Netherlands

¹⁰ Faculty of Mathematics and Physics, University of Ljubljana, Jadranska 19, 1000 Ljubljana, Slovenia

19 June 2022

ABSTRACT

Recent X-ray observations of galaxy clusters show that the distribution of intra-cluster medium (ICM) metallicity is remarkably uniform in space and in time. In this paper, we analyse a large sample of simulated objects, from poor groups to rich clusters, to study the dependence of the metallicity and related quantities on the scale of systems. The simulations are performed with an improved version of the Smoothed-Particle-Hydrodynamics GADGET-3 code and consider various astrophysical processes including radiative cooling, metal enrichment and feedback from stars and active galactic nuclei (AGN). The scaling between the metallicity and the temperature and its evolution obtained in the simulations agrees well with the observational results obtained from two data samples characterised by a wide range of masses and a large redshift coverage. We find that at present time ($z = 0$) the iron abundance in the cluster core ($r < 0.1R_{500}$) does not correlate with the temperature and does not present a significant evolution. The scale invariance is confirmed when the metallicity is related directly with the total mass. The slope of the best-fitting relations is shallow ($\beta \sim -0.1$) in the innermost regions ($r < 0.5R_{500}$) and consistent with zero outside. We investigate the impact of the AGN feedback and find that it plays a key role in producing a constant value of the outskirts metallicity from groups to clusters. This finding additionally supports the picture of early enrichment.

Key words: galaxies: clusters: general — galaxies: clusters: intracluster medium — X-ray: galaxy: clusters — methods: numerical

1 INTRODUCTION

Being the largest gravitationally-bound objects in the Universe, galaxy clusters are considered as closed boxes which contain a fair representative of the cosmic baryon content (White et al. 1993, Frenk et al. 1999). Therefore they are ideal laboratories to study the cosmic cycle of the baryonic matter in its various phases: hot intra-cluster medium (ICM), cold gas, and stellar component. The first component, the ICM, emits dominantly in the X-ray band due to its

high temperature ($T \sim 10^7 - 10^8$ K), making X-ray observations a key tool to study thermodynamics of the ICM (see Böhringer and Werner 2010 for a review). Furthermore, emission-line features of the X-ray observed spectra also reveal wealth of information about the chemical composition of the intra-cluster gas, whereby offering a unique window to study the ICM metal enrichment (Werner et al. 2008).

The ICM metal enrichment involves numerous astrophysical processes (see, e.g., Borgani et al. 2008 for a review). Metals, elements that are heavier than H and He, are created via stellar nucleosynthesis and released by means of stellar mass loss of low- and

* truongnhut@caesar.elte.hu

† Einstein and Spitzer Fellow

intermediate-mass stars or of supernova (SN) explosions. Different types of supernovae produce different elements. The core-collapse or Type II supernovae (SNII) produce mainly light elements, e.g. O, Ne, Mg, or Si, while Type-Ia supernovae (SNIa) are source of heavy metals: Fe and Ni. The intermediate-mass elements are produced by both types of supernovae, and lighter elements (C, N) originate from low- and intermediate-mass stars during their Asymptotic Giant Branch (AGB) phase. The produced metals subsequently enrich the surrounding astrophysical environment thanks to multi-scale mixing processes, such as galactic winds, AGN feedback, ram-pressure stripping, and mergers (see [Schindler and Diaferio 2008](#) for a review). In particular, X-ray observations show evidences that AGN outflows can eject metals up to several 100 kpc even in massive galaxy clusters and groups (e.g., [Kirkpatrick et al. 2011](#); [Ettori et al. 2013](#)). This phenomenon is reproduced in high-resolution hydrodynamical simulations as well (e.g., [Gaspari et al. 2013](#)).

Despite the astrophysically complex nature of the ICM metal enrichment, recent X-ray observations have shown that the distribution of metals in the ICM is remarkably homogeneous in space ([Werner et al. 2013](#); [Urban et al. 2017](#)) and in time ([Ettori et al. 2015](#); [McDonald et al. 2016](#)). [Werner et al. \(2013\)](#) and [Urban et al. \(2017\)](#) show that the iron profile in the ICM of the Perseus cluster and other ten clusters observed by Suzaku is flat at radii $r > 0.25R_{200}^1$ with an iron abundance level of $\sim 0.3 Z_{Fe,\odot}$. In another work, [McDonald et al. \(2016\)](#), based on X-ray observations of 153 clusters observed by *Chandra*, *XMM-Newton*, and *Suzaku* telescopes, reveal no evidence for strong redshift evolution of the global ICM metallicity ($r < R_{500}$) (see also [Ettori et al. 2015](#)). Even more interestingly, recent observation of Perseus cluster from *Hitomi* ([Hitomi Collaboration et al. 2017](#)) shows that the chemical composition of the ICM is consistent with the solar chemical composition.

Numerical modelling also supports the uniform picture of ICM metal enrichment. In recent studies based on simulations, [Biffi et al. \(2017, 2018\)](#) and [Vogelsberger et al. \(2017\)](#) also find a flat metallicity profile in cluster outskirts that is constant over time. The uniformity of ICM metallicity in space and time supports the picture of early metal enrichment. In this scenario, early-time pristine gas in galaxies was enriched at high redshift ($z \sim 5 - 6$) and then widespread mainly by feedbacks. The gas was subsequently accreted into massive halos and heated due to gravitational compression. Since the gas was already metal-rich at the time of accretion, the ICM metallicity profile appears to be flat at large cluster-centric distances.

In addition to a flat and constant metal distribution, the early enrichment scenario can be tested by investigating the mass dependence of the metallicity. For this, there is recently interest from both theoretical ([Yates et al. 2017](#); [Vogelsberger et al. 2017](#); [Barnes et al. 2017](#)) and observational ([Mantz et al. 2017](#); [Yates et al. 2017](#)) sides in investigating how the ICM metallicity varies with cluster scale. Up to date, the most complete observed sample, for the study of averaged ICM metallicity in clusters, has been carried out by [Mantz et al. \(2017\)](#). This work shows that iron abundance in the ICM anti-correlates with ICM temperature, however, the study is limited to a massive sample only ($T > 5$ keV). An earlier work from [Yates et al. \(2017\)](#), based on a compilation of various observa-

tional datasets from the literature, reports a similar anti-correlation between iron abundance and temperature in high-temperature systems, while in low-temperature systems ($T < 1.7$ keV) the compiled sample exhibits a drop in the iron abundance (see also, [Sun 2012](#); [Mernier et al. 2016](#)). This drop is not present in recent numerical studies (e.g., [Yates et al. 2017](#)).

In this paper we carry out a thorough study on how ICM metallicity varies (1) from group to cluster scales, (2) in various radial ranges and (3) in time, by employing cosmological hydrodynamical simulations.

The simulated sample that we analysed is the one presented in [Biffi et al. \(2017, 2018\)](#). This set of simulated clusters has also been shown to reproduce various realistic thermodynamical properties of the ICM ([Rasia et al. 2015](#); [Villaescusa-Navarro et al. 2016](#); [Biffi et al. 2016](#); [Planelles et al. 2017](#); [Truong et al. 2018](#)).

In the first part of this study, we present a comparison between simulations and observations on the dependence of the ICM metallicity on the gas temperature, in which specific attention is paid to potential biases that might affect the observational results. In particular, the observational datasets that we use include the CHEERS sample observed by *XMM-Newton* telescope ([de Plaa et al. 2017](#)), in which the X-ray spectra are analysed with the last up-dated model of ICM emission for metallicity estimation. The detailed description of the CHEERS data as well as its X-ray analysis is provided in a companion paper (Mernier et al., submitted). In addition, we also compare our simulation results against recent observational data by [Mantz et al. \(2017\)](#).

In the second part, we theoretically investigate how the metallicity varies as a function of cluster mass as well as how this relation evolves over redshift. In order to enhance the role played by AGN feedback on the early enrichment, we study how the iron mass, hydrogen mass and stellar fraction relate with the total mass in simulations with and without AGN feedback.

The paper is organized in the following way. We describe the main features of the numerical simulation and the method of analysis in Section 2. In Section 3, we briefly introduce the observed datasets: the CHEERS ([de Plaa et al. 2017](#)), and [Mantz et al. \(2017\)](#) samples. This is followed by a detailed comparison between simulations and observations. In Section 4, we present theoretical investigation on the iron and oxygen abundance-mass relations as well as its evolution over time. The effects of AGN feedback on the mass-metallicity relation, and related quantities, are also discussed in this Section. Finally, we summarise the main results and conclude in Section 5.

Throughout this study, we adopt the solar metallicity values provided by [Asplund et al. \(2009\)](#) for both the theoretical and the observational analysis and we consider $h \equiv H_0/100\text{km/s/Mpc} = 0.72$, where H_0 is the Hubble constant.

2 ANALYSIS OF SIMULATIONS

2.1 The Simulated Clusters

The simulations employed in this study have been described in recent works ([Rasia et al. 2015](#); [Villaescusa-Navarro et al. 2016](#); [Biffi et al. 2016](#); [Planelles et al. 2017](#); [Biffi et al. 2017, 2018](#); [Truong et al. 2018](#)), where we show that they reproduce consistent chemo- and thermo-dynamical cluster properties in comparison to observational data.

In this Section we summarise only the main features and refer the reader to the aforementioned references for more details, and

¹ The mass enclosed within a sphere that has averaged density equal to 200 times the critical density of the Universe (ρ_{crit}). In general, the mass M_Δ is related to the radius R_Δ by the equation: $M_\Delta = 4\pi\Delta\rho_{\text{crit}}R_\Delta^3$. We also use R_{500} and R_{2500} in this work.

specifically to Biffi et al. (2017) for the description of how chemical enrichment is included in the simulations.

The simulated galaxy clusters are obtained from 29 zoomed-in Lagrangian regions re-simulated with an upgraded version of the GADGET-3 code (Springel 2005). Starting from an initial Dark-Matter (DM) only simulation with a volume of $(1h^{-1}\text{Gpc})^3$, 24 regions around halos with $M_{200} > 8 \times 10^{14}h^{-1}M_{\odot}$, and 5 regions around smaller halos with $M_{200} \sim [1 - 4] \times 10^{14}h^{-1}M_{\odot}$ are selected and re-simulated at higher resolution and with added baryonic components (see Bonafede et al. 2011 for more details on the initial conditions). The mass resolutions for DM and gas particles are $m_{DM} = 8.47 \times 10^8 h^{-1}M_{\odot}$, $m_{gas} = 1.53 \times 10^8 h^{-1}M_{\odot}$, respectively. The simulation is performed with cosmological parameters: $\Omega_m = 0.24$, $\Omega_b = 0.04$, $n_s = 0.96$, and $\sigma_8 = 0.8$. The Plummer-equivalent softening length is fixed equal to $\epsilon = 3.75h^{-1}\text{kpc}$ for DM and gas particles, and $\epsilon = 2h^{-1}\text{kpc}$ for black hole and star particles. The DM softening length is fixed in comoving units for $z > 2$ and in physical units at lower redshift. For other types of particles, it is always given in comoving units.

Regarding the hydrodynamical scheme, we employ the improved Smoothed-Particle-Hydrodynamics (SPH) formulation described in Beck et al. (2016). Comparing to the standard GADGET code, the new SPH scheme incorporates a number of advanced features including: the choice of a higher-order Wendland C^4 kernel function, the implementation of a time-dependent artificial viscosity scheme, and artificial conduction. These advanced features improve the scheme's ability in treating contact discontinuities and gas-dynamical instabilities, thereby overcoming several limitations of standard SPH schemes.

For the study of metallicity of the intra-cluster gas, we adopt two different prescriptions for the ICM physics which have been used to produce two simulated samples from the same initial conditions. The run called CSF (cooling-star-formation) includes the following physical processes:

- Heating/cooling from Cosmic Microwave Background (CMB) and from a UV/X-ray time-dependent uniform ionising background included as in Haardt and Madau (2001).
- Metallicity-dependent radiative gas cooling as in Wiersma et al. (2009), and star formation (Springel and Hernquist 2003).
- Metal enrichment, as described in Tornatore et al. (2007), accounting for three different channels of enrichment, namely from SNII, SNIa, and AGB stars. We follow the production and evolution of 15 different chemical species: H, He, C, Ca, O, N, Ne, Mg, S, Si, Fe, Na, Al, Ar, Ni. We assume the stellar initial mass function (IMF) by Chabrier (2003), and the mass-dependent lifetimes of Padovani and Matteucci (1993). The stellar yields used in the model are the set provided in Thielemann et al. (2003) for SNIa stars and the one from Karakas (2010) for AGB stars. For SNII, we use the metal-dependent yields taken from Woosley and Weaver (1995) and Romano et al. (2010).
- Thermal feedback from supernovae as originally prescribed by Springel and Hernquist (2003). Kinetic feedback from the SN is also included, in the form of galactic winds with a velocity of 350 km s^{-1} .

The other run is called AGN. It has all the features of the CSF run but additionally includes the treatment of gas accretion onto super-massive black holes (SMBH) powering AGN feedback, for which we employ the model by Steinborn et al. (2015) (an upgrade from the original model proposed by Springel et al. 2005) that considers both hot and cold accretion (e.g., Gaspari et al. 2018).

For this study, we select only systems with mass $M_{500} > 2 \times$

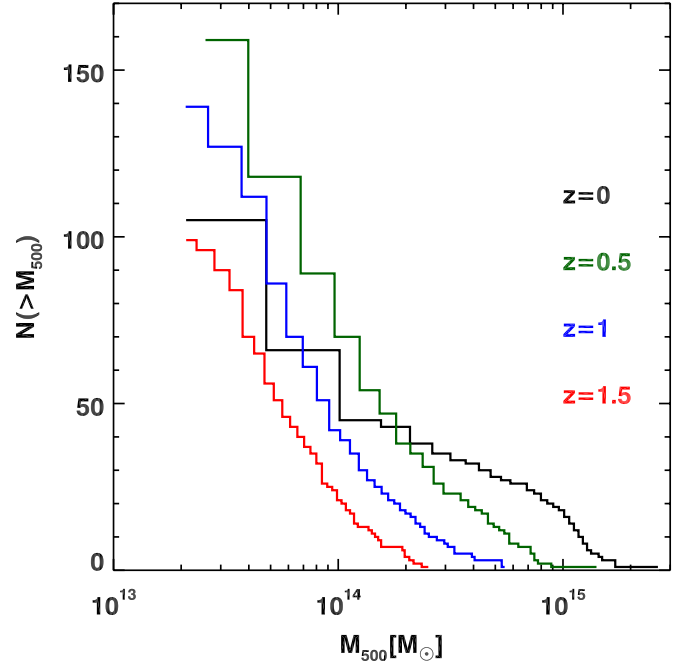


Figure 1. The cumulative distribution of M_{500} in our AGN simulation at different redshifts for those objects with $M_{500} > 2 \times 10^{13}M_{\odot}$ and having at least 100 gas particles in the core ($r < 0.1R_{500}$).

$10^{13}M_{\odot}$, that have at least 100 gas particles in the central regions ($r < 0.1R_{500}$) in order to robustly quantify global quantities also in the cluster core. In Fig. 1 we show the cumulative distribution of cluster total mass, in terms of M_{500} , at the four redshifts, $z = 0, 0.5, 1$, and 1.5 , that we will consider in this work.

2.2 Computing simulated ICM quantities

In the following we briefly describe how quantities of interest are computed within the simulation snapshots.

• *Projected quantities.* For the purpose of comparing simulation results with observational data, we employ projected quantities. Namely, we compute the temperature and the metallicity within a cylindrical volume with the length of $2 \times R_{vir}$, where R_{vir} is the virial radius², and the area confined by two circular apertures. In order to be consistent with X-ray observations, which are typically centred on the surface brightness peak, we center the cylindrical regions on the center of the gas mass calculated from the gas particles within R_{2500} (which is typically $\sim 0.3R_{500}$).

For the temperature, we adopt the spectroscopic-like formula proposed by Mazzotta et al. (2004):

$$T_{st} = \frac{\sum_i \rho_i m_i T_i^{0.25}}{\sum_i \rho_i m_i T_i^{-0.75}}, \quad (1)$$

where m_i , ρ_i , and T_i are the mass, density, and temperature of the i^{th} gas element, respectively. For the computation of spectroscopic-like temperature, we apply a temperature cut $T_i > 0.3 \text{ keV}$ to select particles that should emit in the X-ray band.

² For the cosmology used in our simulations, the virial radius corresponds to $\Delta \approx 93$ at $z = 0$.

For the metallicity, we adopt the *emission-weighted* estimate, defined as:

$$Z_{ew} = \frac{\sum_i n_{e,i} n_{H,i} \Lambda(T_i, Z_i) \times Z_i}{\sum_i n_{e,i} n_{H,i} \Lambda(T_i, Z_i)}, \quad (2)$$

where Z_i is the gas particle metallicity, and $n_{e,i}$, $n_{H,i}$ are the electron and hydrogen number densities, respectively. Λ is the cooling function computed based on particle temperature and metallicity by assuming the APEC model (Smith et al. 2001) in XPEC for radiative emission and by integrating over the [0.01 – 100] keV energy band.

- *Theoretical estimates.* For the theoretical investigation of the simulated clusters, we use three-dimensional measurements, computed within spherical shells centred on the minimum of the system potential well.

For the iron and oxygen abundances we employ the *mass-weighted* formula, defined as:

$$Z_{mw} = \frac{\sum_i m_i \times Z_i}{\sum_i m_i}, \quad (3)$$

where m_i is the gas particle mass, and Z represent one of the two elements.

Similarly, to explore the intrinsic dependence of ICM metallicity on the cluster scale and related quantities, we also measure total, iron and hydrogen masses, as well as stellar fractions, evaluated within spherical three-dimensional regions.

2.3 Fitting Method

We model the relations between metallicity, total mass or temperature, and redshift with power-law functional forms. The specific function adopted will be specified, case by case, in the following sections. In order to characterise the slope and normalisation of the relations, we always perform a log-log linear regression fit. For this task, we employ the IDL routines `linmix_err.pro` and `mlinmix_err.pro` which adopt a Bayesian approach to linear regression as described in Kelly (2007). This method enables us to treat the intrinsic scatter as a free parameter, like the slope and normalisation, and it is determined via the method of Monte Carlo Markov Chains (see Kelly 2007 for detailed discussion).

3 COMPARISON TO OBSERVATIONS

In the first part of this study we investigate the iron abundance in simulated and observed clusters as function of ICM temperature. In fact, even though the mass is the optimal representative of the system scale, this quantity is not directly observable and temperature measurements, which are easier to derive, are typically used in X-ray studies. For the purpose of a more faithful comparison to observational data, we therefore employ projected spectroscopic-like temperature estimates of the ICM in simulated clusters as well. We note that the relation between temperature and mass for the clusters in our AGN simulations is in good agreement with observational findings, both at low and intermediate redshifts (Truong et al. 2018).

3.1 Observational Data Sets

In the following we briefly describe the main features of the two observational datasets used for the comparison with simulation results, namely the CHEERS sample and the sample presented in

Mantz et al. (2017). Specifically, we will take advantage of the large temperature range spanned by the former, a local cluster sample, in order to investigate in detail the dependence of central metallicity on core temperature in local clusters. For the purpose of exploring the redshift evolution of the metallicity-temperature relation, in different radial ranges, we will use instead the latter, which contains a larger number of massive clusters.

- The CHEERS sample includes 43 nearby ($z < 0.1$) cool core clusters, groups, and massive ellipticals observed by *XMM-Newton*. The iron abundance is constrained by the *XMM-Newton* EPIC (MOS 1, MOS 2, and pn) instruments, as they can access both the Fe-L and the Fe-K line complexes of the X-ray spectral window. We use the Fe measurements from Mernier et al. (submitted), which are derived within $0.1R_{500}$ and obtained from fitting X-ray spectra using the up-to-date version of the spectral code used to model the ICM emission, namely SPEXACT³. A major update has been recently released (i.e. from SPEXACT v2 to SPEXACT v3, de Plaa et al. 2017) and, compared to the previous observational results, SPEXACT v3 revises the Fe abundance in groups significantly higher and makes them on average consistent with that in clusters. In order to minimise the impact of the Fe-bias, all the spectra were fitted with three single-temperature components that mimic a Gaussian temperature distribution. The complete details and discussion on the data analysis methods and the effects of the latest spectral model improvements are presented in Mernier et al. (submitted).

- The sample by Mantz et al. (2017) is the largest sample available up-to-date. It consists of 245 massive systems ($T > 5$ keV) selected from X-ray and Sunyaev-Zel'dovich effect surveys, with X-ray observations obtained from *Chandra*. The sample encompasses a broad redshift range: $0 < z < 1.2$. Metallicity analysis is performed for three radial ranges: $[0 - 0.1]R_{500}$, $[0.1 - 0.5]R_{500}$, and $[0.5 - 1]R_{500}$.

3.2 The $Z_{Fe} - T$ relation for groups and clusters

In Fig. 2 we show the $Z_{Fe} - T$ relation measured within $0.1R_{500}$ for the AGN simulated sample in comparison to the CHEERS data set. Since the this sample includes only nearby objects, we consider only $z = 0$ simulated clusters. In addition, to be consistent with the data, we select simulated systems that have temperature greater than 0.7 keV at $z = 0$. To characterise the correlation between Z_{Fe} and T , we compute the Spearman's rank correlation coefficients (r_s) for simulated and observed samples. Additionally, we also quantify the dependence of iron abundance on temperature by fitting the simulated and the observed data with the following formula:

$$Z_{Fe} = Z_{0T} \left(\frac{T}{1.7 \text{ keV}} \right)^{\beta_T}, \quad (4)$$

which is characterised by two parameters: the normalisation Z_{0T} and the slope β_T . We choose the pivotal point for the temperature equal to 1.7 keV, which is close to the mean values of the simulated and observed sample temperatures. The correlation coefficients r_s and the best-fitting parameters of Eq. (4) are reported in Table 1.

Both simulations and observations show almost no correlation ($|r_s| \leq 0.2$) between the iron abundance and the temperature in

³ SPEX Atomic Code and Tables, as part of the fitting package SPEX (<https://www.sron.nl/astrophysics-spx>).

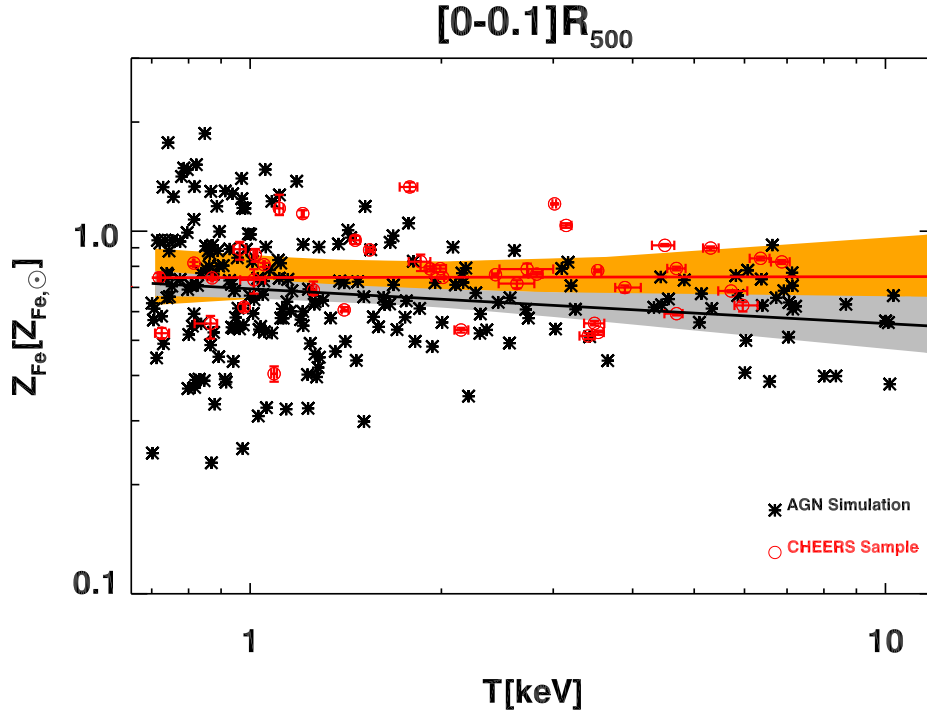


Figure 2. Comparison between the AGN simulated $Z_{Fe} - T$ relation and the observational data from the CHEERS sample. The iron abundance and temperature are measured within $0.1R_{500}$. Solid lines represent the best-fitting relations, while the shaded regions represent the 68.3% confidence regions.

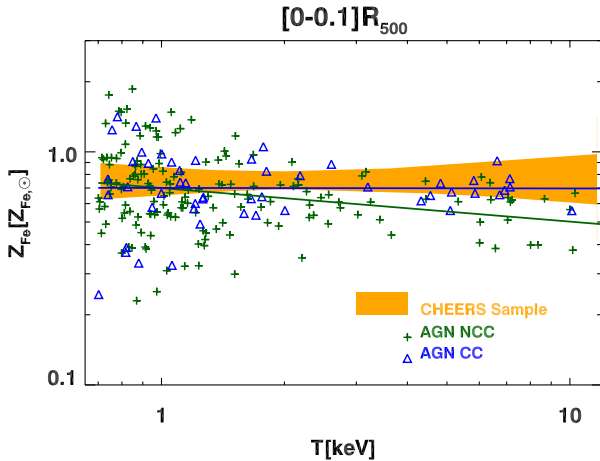


Figure 3. $Z_{Fe} - T$ relation for simulated CC (blue triangles) and NCC (green crosses) subsamples shown along with their best-fit relations (solid lines). The orange area is the 68.3% confidence region for the CHEERS sample as shown in Fig. 2.

the cluster core. The CHEERS data show a flat distribution of iron abundance across the temperature range with the slope β_T consistent with zero within the uncertainty. The relation for our simulated data also presents a very shallow slope $\beta_T \sim -0.1$, which implies that, on average, a cluster that is 10 times hotter than a group has only about 20% lower metallicity. This indicates that the ICM iron abundance is statistically constant from groups to clusters in the entire sample.

Compared to the CHEERS sample, the iron abundance of the simulated objects with $T \geq 2$ keV is slightly lower than the observed value at a given temperature. At the pivotal point of temper-

ature, 1.7 keV, the observed Z_{Fe} is higher than the simulated one by 13%, yet the two values are consistent given the intrinsic scatter. The slight offset in normalisation is related to various factors including the details of the model for chemical enrichment used in the simulation, e.g. the stellar initial mass function and the sets of yields. Another source which may cause the discrepancy is the difference in the sample selection, as the CHEERS sample is exclusively composed by cool-core objects. We will discuss this aspect in the following section.

We note that the simulated data exhibit slightly higher scatter ($\sigma \log_{10} Z_{Fe}|T = 0.16$) than the observed CHEERS data ($\sigma \log_{10} Z_{Fe}|T = 0.11$). It is evident from Fig. 2 that the larger scatter in simulated data could mainly be due to the larger statistics of low-temperature groups ($T < 1.7$ keV). In simulations, these systems have small radius (the mean $R_{500} \sim 450$ kpc) so that the level of metallicity in the central region ($< 0.1R_{500}$) is very sensitive to AGN feedback, the efficiency of radiative cooling, and the dynamical state of the system.

3.2.1 Cool-core and non-cool-core $Z_{Fe} - T$ relations

Cool-core clusters are shown to host larger amount of metals in the core region compared to non cool-core clusters (e.g. De Grandi et al. 2004). Therefore we might expect a difference between the CC and the NCC $Z_{Fe} - T$ relations that need to be evaluated to estimate any potential bias in observed samples. This is particularly relevant for the CHEERS sample as its member clusters are selected by RGS (the Reflection Grating Spectrometer onboard *XMM-Newton*) which is selectively sensitive to centrally-peaked clusters (de Plaa et al. 2017) and the peakiness is considered as “proxy” of the cool-core-ness (e.g. Mantz et al. 2017). To address this issue, we divide the simulated AGN dataset into cool-core and non cool-core subsamples, and study the iron abundance-

temperature relation for each of them separately. For the selection of simulated CC systems, we compute the pseudo-entropy defined as:

$$\sigma = \frac{(T_{IN}/T_{OUT})}{(EM_{IN}/EM_{OUT})^{1/3}}, \quad (5)$$

where T is the spectroscopic-like temperature and EM is the emission measure, computed in the IN region, $r < 0.05 \times R_{180}$, and OUT region, $0.05 \times R_{180} < r < 0.2R_{180}$. Following [Rasia et al. \(2015\)](#) we define CC systems those that have a pseudo-entropy value lower than 0.55, whereas systems with $\sigma > 0.55$ are classified as NCC. We show in Fig. 3 the $Z_{Fe} - T$ relation for both the CC and NCC subsamples along with the CHEERS data.

In general the CC systems have slightly higher central iron abundance, e.g. $\sim 8\%$ at 1.7 keV, than the NCC ones, which is consistent with recent numerical and observational studies showing that the ICM iron profile in CC clusters is steeper and peaked in the central regions ([Leccardi et al. 2010](#); [Rasia et al. 2015](#); [Ettori et al. 2015](#); [Biffi et al. 2017](#)). However, the difference is for temperature $T > 2$ keV, while for low-temperature systems, the separation between the metallicity level in CCs and NCCs is not well-established and the scatter is large. As a consequence, the slope of the $Z_{Fe} - T$ of CCs is flatter than that of NCCs. Hence, for the study of $Z_{Fe} - T$ relation, the effect of solely including CC systems mainly affects the slope of the high-temperature end, whereas the effect is not very significant in the low-T regime.

The CC subsample is in better agreement with the CHEERS dataset than the NCC subsample, not only in terms of the slope, $\beta_T \sim 0$, but also in terms of the normalisation. The cores of both simulated CC and observed clusters present a constant iron abundance equal to $Z_{Fe} \simeq 0.75Z_{Fe,\odot}$ over the considered range of temperature with a dispersion of $\sim 40\%$ and $\sim 30\%$, respectively.

3.3 $Z_{Fe} - T$ evolution in massive clusters

In this subsection we compare the AGN simulated $Z_{Fe} - T$ relation with the result obtained by [Mantz et al. \(2017\)](#) for massive clusters. To be consistent with them, we select simulated clusters with $T_{[0.1-0.5]R_{500}} > 5$ keV, where $T_{[0.1-0.5]R_{500}}$ is the temperature measured within the region $[0.1 - 0.5]R_{500}$. We consider 6 different snapshots corresponding to redshifts: $z = 0, 0.25, 0.5, 0.6, 0.8$, and 1, where we, respectively, identify 26, 19, 10, 11, 6, and 2 objects. For this comparison, we use the projected emission-weighted iron abundance and the spectroscopic-like temperature computed within three radial ranges: $[0 - 0.1]R_{500}$, $[0.1 - 0.5]R_{500}$, and $[0.5 - 1]R_{500}$. Following the approach by [Mantz et al.](#), we quantify the correlation between Z_{Fe} and T in addition to study the evolution of the relation by simultaneously fitting all simulated data by the formula:

$$Z_{Fe} = Z_{0T} \times \left(\frac{1+z}{1+z_{piv}} \right)^{\gamma_z} \times \left(\frac{T}{T_{piv}} \right)^{\beta_T}, \quad (6)$$

where the free parameters are: the normalisation Z_{0T} , the slope β_T , and the redshift evolution of the iron abundance, γ_z . We fix the pivot values of redshift and temperature, z_{piv} and T_{piv} , to the same values used in the observational analysis reported in Table 2, where we also list the best-fitting parameters of the $Z_{Fe} - T$ relation from our analysis as well as from the work of [Mantz et al. \(2017\)](#) (see their Table 1).

As shown in Fig. 4, the simulation radial trends of the iron abundance are consistent with the data over the three considered

radial ranges. On average, both simulated and observed iron abundance are higher in the innermost region, where $Z_{Fe} \sim 0.6Z_{Fe,\odot}$, and they gradually decrease to the level of $0.2Z_{Fe,\odot}$ in the most external radial range. This result is in line with previous works on ICM metallicity profiles from both simulations and observations (e.g. [Werner et al. 2013](#); [Rasia et al. 2015](#); [Urban et al. 2017](#); [Biffi et al. 2017, 2018](#)).

The simulations also agree well with the analysis by [Mantz et al.](#) on the $Z_{Fe} - T$ intrinsic scatter. Among the three considered radial ranges, both simulations and observations present the largest scatter in the core (see Table 2), that is strongly affected by several astrophysical processes such as feedback from the AGN, or intense stellar activity.

In terms of the slopes, we notice a good agreement between simulations and observations in the two regions within half of R_{500} , while the best-fitting lines seem to have opposite trends in the cluster outskirts ($\beta_{sim} = -0.47$ and $\beta_{obs} = 0.22$). However, the observational constraints are weak and considering the 1σ error associated with β_{obs} , equal to 0.34, the two slopes are consistent within 2σ . In addition, most of the simulated points are well within the shading area showing the observational 1σ dispersion around the best-fitting line.

It is interesting to note that the negative slopes of the simulation data are affected by the specific selection of the hottest clusters as illustrated in Fig. 5, where the best-fitting relation of the most massive sample (red line) is compared with the overall trend (black line). In particular, the steep relation that characterises the core of the massive simulated clusters is biased by the segregation between the CC and NCC systems: the CCs have both higher metallicity and lower temperature compared to the NCCs. This separation disappears when the groups are added to the sample (see also Fig. 3).

Finally, the evolution of the $Z_{Fe} - T$ relation is positive in all radial ranges: at fixed temperature, the iron abundance increases with time (see γ_z values in Table 2). The amplitude of this variation is however limited, as the iron abundance on average grows by less than 30% from $z = 1$ to $z = 0$. This result is consistent with other observational analyses ([Ettori et al. 2015](#); [McDonald et al. 2016](#)). As for the radial trend of the evolution, the simulated data show that the normalisation of the $Z_{Fe} - T$ relation evolves almost equally in the three radial ranges, while the observed data by [Mantz et al. \(2017\)](#) exhibit a stronger evolution of the iron abundance, with $\gamma_z = -0.71 \pm 0.15$ in the intermediate radial range. The authors suggest that the late-time increase of iron abundance of the gas in the intermediate radial range could be due to the mixing with enriched gas from the cluster centers caused by mergers or AGN outflows. Observational results on the spatial pattern of metallicity evolution is, however, still matter of debate. At variance with the conclusions by [Mantz et al. \(2017\)](#), [Ettori et al. \(2015\)](#) show that the ICM metallicity slightly evolves in the central region of the CC clusters only and, even in these objects, it remains constant at larger radii. On the other hand, [McDonald et al. \(2016\)](#) point out that the ICM metallicity is consistent with no evolution outside of the core.

4 MASS-METALLICITY RELATION AND EVOLUTION

One of the goals of this paper is to check whether the metallicity distribution and evolution is scale invariant. In observational data the temperature is used as mass-proxy, however, since both temperature and metallicity are derived from the same spectra there is a certain degeneracy between the two quantities. Furthermore, the measurements of the temperature in the central regions can be

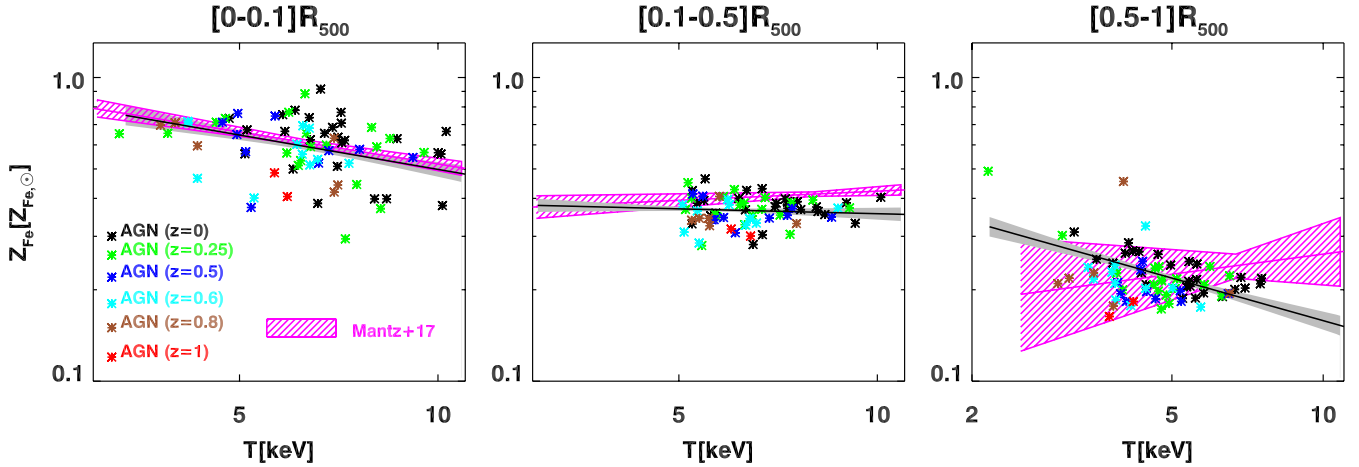


Figure 4. Comparison between the AGN simulated $Z_{Fe} - T$ relation and the observational results from Mantz et al. 2017 within different radial ranges for massive systems ($T_{[0.1-0.5]R_{500}} > 5$ keV). The AGN best-fit relation is represented with a black solid line and the grey-shaded area specifies the 68.3% confidence region. The observational constraint region, which is confined between the two magenta curves, is derived based on the best-fit values of normalisation and slope and their associated 1σ uncertainties (see Table 2). The simulated and observed best-fit relations are evaluated at the pivot redshift and temperature as reported in Table 2.

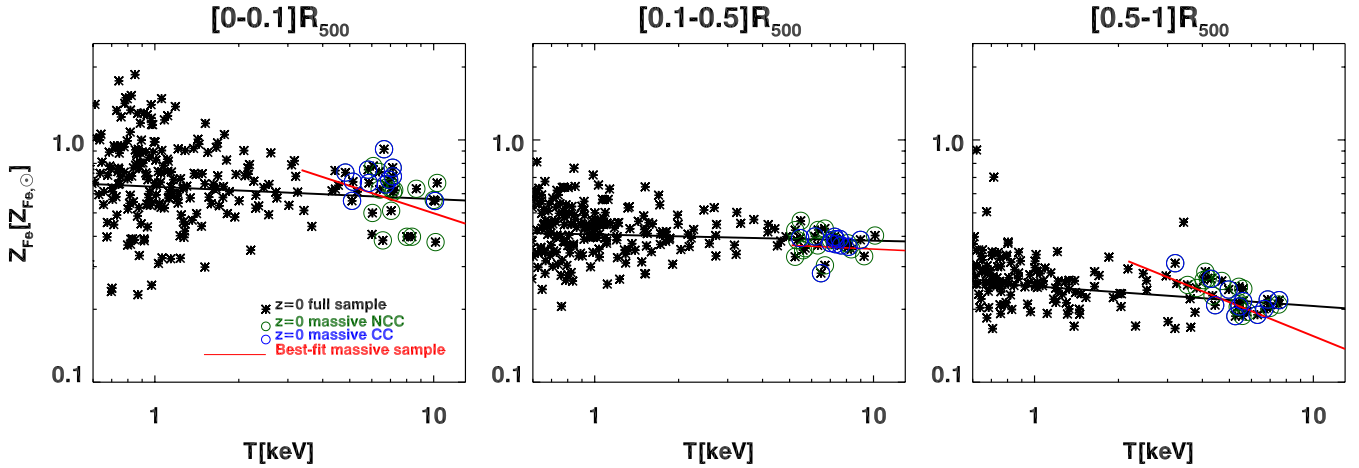


Figure 5. Comparison between the $Z_{Fe} - T$ simulated relations at $z = 0$ derived from the entire sample and the massive subsample. The circles specify massive clusters that are selected according to their temperature $T_{[0.1-0.5]R_{500}} > 5$ keV. Green circles are NCC and the blue ones are CC systems. The solid lines are best-fitting relations corresponding to the whole sample at $z = 0$ (black) and to the selected massive sample from $z = 0$ to $z = 1$ (red).

biased low because of multi-temperature gas. In the previous section we mimic the spectral measurements of metallicity and temperature by using projected quantities and we showed agreement between the simulated and observed data. In this section, we take advantage of the precise knowledge of the mass from simulations and we study how the distribution and evolution of metallicity depends on the total mass (M_{500}) and how this trend is influenced by the presence of the AGN. At first, we will analyse the dependence of both iron and oxygen, while in the second part we will focus exclusively on the iron because the two metal elements present very similar behaviours. All relations are extended to poor groups, $M_{500} \sim 2 - 3 \times 10^{13} M_{\odot}$, satisfying the condition reported at the end of Section 2.1.

4.1 The $Z_{Fe} - M_{500}$ and $Z_O - M_{500}$ relations

The relationship between Z_{Fe} , Z_O and M_{500} is computed within the same apertures as before with the addition of one more external region: $[1 - 2]R_{500}$. The relations are evaluated separately at four fixed redshifts: $z = 0, 0.5, 1$, and 1.5 . In a second time we quantify the evolution of the relation combining the samples.

To characterise the mass-metallicity relations, we fit the simulated data extracted in a given radial range and at a particular time, to a formula similar to Eq. (4):

$$Z_X = Z_{0,X} \times \left(\frac{M_{500}}{10^{14} M_{\odot}} \right)^{\beta_X}, \quad (7)$$

where X stands for iron or oxygen. The best-fitting parameters of the $Z_{Fe} - M_{500}$ and $Z_O - M_{500}$ relations as well as the Spearman's rank correlation coefficients are reported in Table 3 and shown in Fig. 6. In particular, we show in the upper and lower panels the

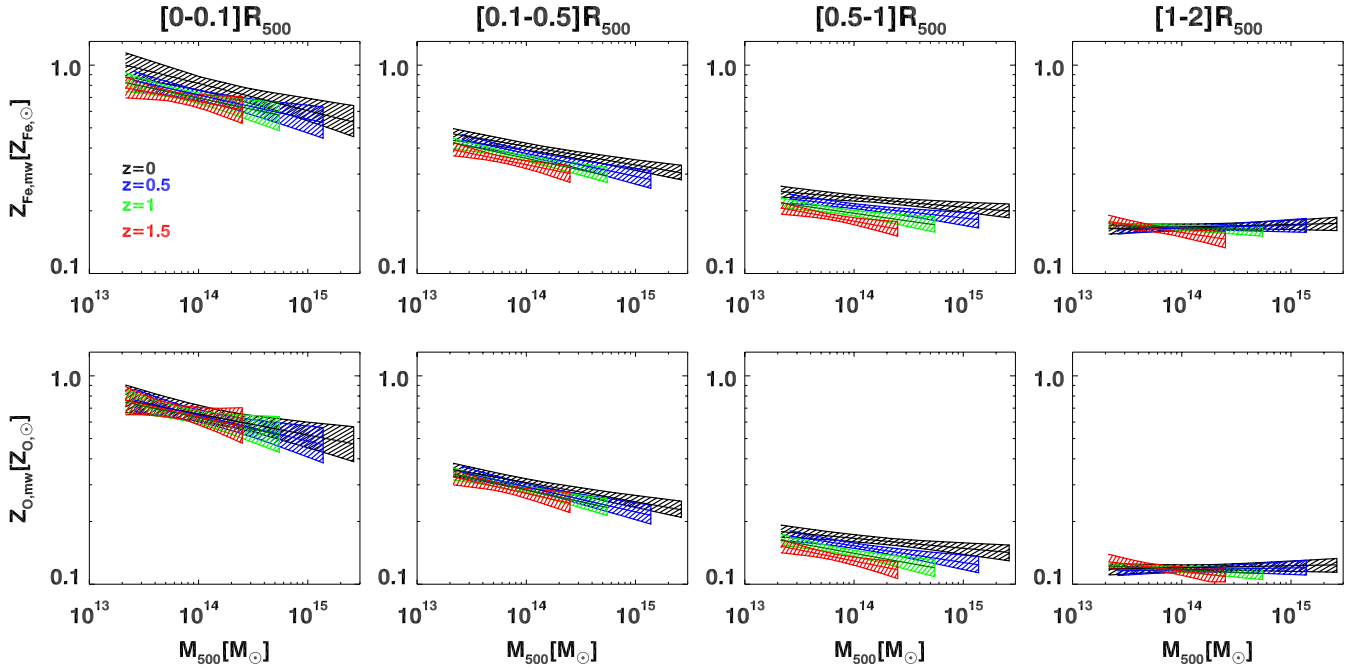


Figure 6. The relation between cluster mass and iron abundance (upper) and oxygen abundance (lower), at different ranges of radius and redshifts. Solid lines are the best-fit relations as described by Eq. (7) with the parameters reported in Table 3, while the line-filled areas specify the 68.3% confidence regions.

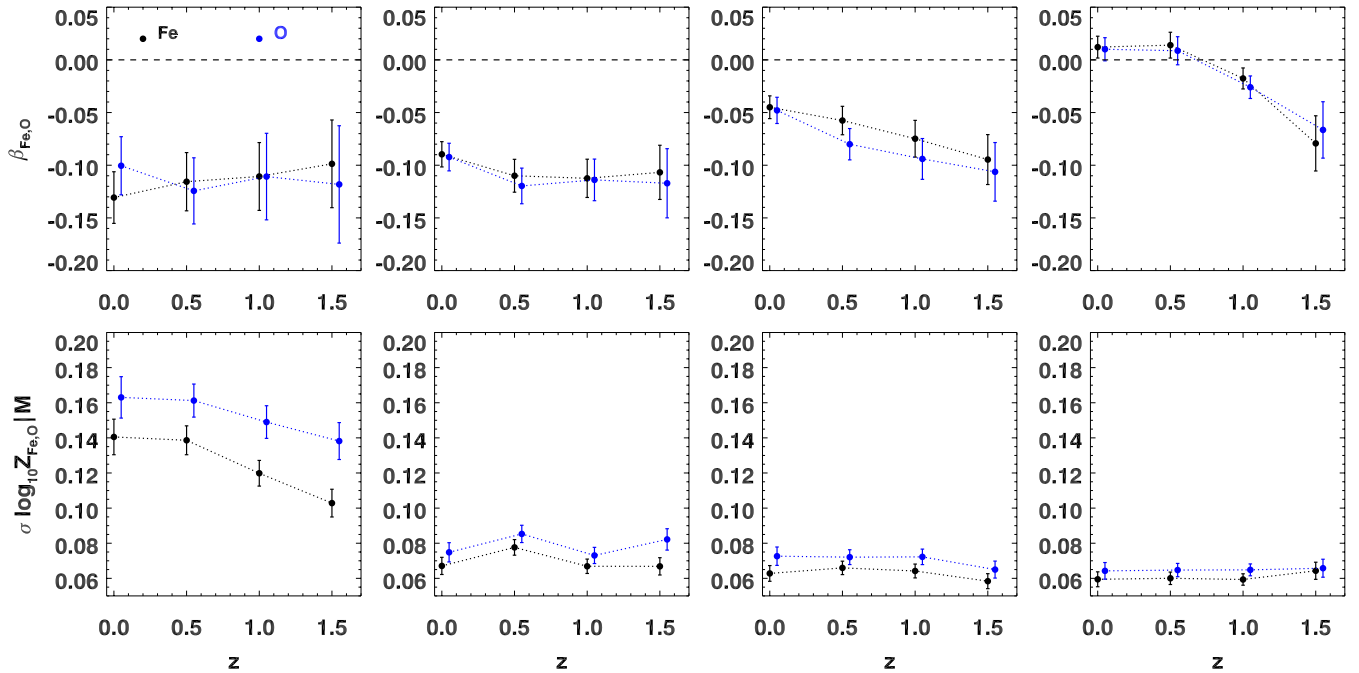


Figure 7. The slope (upper) and scatter (lower) of the $Z_{Fe} - M_{500}$ and $Z_O - M_{500}$ relations as a function of redshift for the four considered radial ranges, from left to right, $[0 - 0.1]R_{500}$, $[0.1 - 0.5]R_{500}$, $[0.5 - 1]R_{500}$, and $[1 - 2]R_{500}$, respectively. The error bars quote 1σ uncertainty.

metallicity-mass best-fitting relations for iron and oxygen, respectively. We include the results for all four apertures and for all times from $z = 0$ to $z = 1.5$.

In general, the behaviour of the two mass-abundance relations are very similar, almost independent of the radial range and redshift at which they are computed. The Spearman's rank correlation coefficients for both relations indicate an anti-correlation

between the metal abundances and the mass in the innermost region ($r < 0.5 \times R_{500}$), especially strong at the lowest redshifts ($z \leq 0.5$), while there is no indication of any mass dependence in the outskirts. However, the slopes of all relations are very shallow ($\beta < -0.15$) everywhere and at anytime (see also Fig. 7). The net difference between a $10^{14}M_{\odot}$ group and a $10^{15}M_{\odot}$ cluster is limited to an abundance decrease of 20-30 per cent. This mild trend is

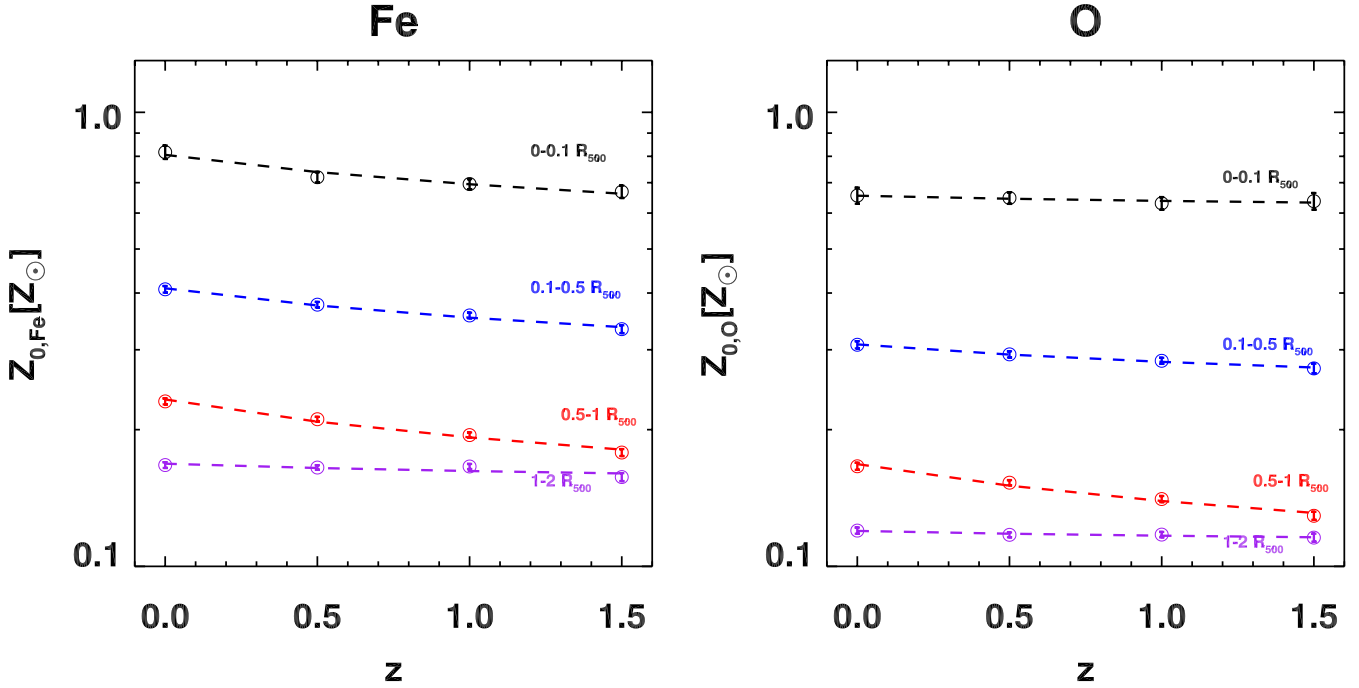


Figure 8. Evolution of the normalisation of the $Z_{Fe} - M_{500}$ (left) and $Z_O - M_{500}$ (right) relations at $M_{500} = 10^{14} M_{\odot}$ for the four considered radial ranges. The dashed-lines represent the best-fit relation as described by Eq. (8) with the parameters reported in Table 4. The error bars quote 1σ uncertainty.

present at any time since β does not substantially vary with redshift as shown in the top panels of Fig. 7.

In the bottom panels of Fig. 7, we report the evolution of the scatter. We notice that the $Z_O - M_{500}$ relation always presents a higher intrinsic scatter than the $Z_{Fe} - M_{500}$. The difference is stronger in the core ($r < 0.1 \times R_{500}$) where it reaches approximately 0.02 – 0.03 dex. With the exception of the difference in amplitude, the trends with radii and time of both scatters are almost identical: the largest values are detected in the core and at most recent times ($\sigma_{\log_{10} Z|M} = 0.14 - 0.16$ dex). Outside that region, both scatters promptly decrease and they remain constant out to the virial region ($\sim 2R_{500}$). The redshift-dependence of the intrinsic scatters is present only in the core where the most important astrophysical processes take place. Specifically, for the iron and the oxygen abundances we respectively find a scatter increase of 37 per cent and 18 per cent from $z = 1.5$ to $z = 0$.

Since the slopes are constant with time at all radii with the exception of a minimal variation in the most external radial bin, we can study the evolution of the relations by simply measuring the shift in the normalisation at a fixed mass that we chose to be equal to $M_{500} = 10^{14} M_{\odot}$. We quantify the evolution in each radial range by fitting the data with the following relation:

$$Z_0(z) = A \times (1 + z)^B. \quad (8)$$

The results are reported in Table 4 and shown in Fig. 8.

The overall metallicity exhibits an extremely weak evolution within R_{500} and no evolution at all in the region between R_{500} and $2R_{500}$. The largest evolution regards the increase by about 25 per cent and 30 per cent of the iron and oxygen abundance, respectively, in the $[0.5 - 1]R_{500}$ region. At redshift 1.5 the normalisations of the iron and oxygen are already very close to the $z = 0$ levels. To be precise, in the four radial ranges from the core to the virial

radius, the iron normalisation at $z = 1.5$ amounted to 92, 85, 77, 100 per cent of its value at $z = 0$. The level of the oxygen is even less evolving since its normalisation is almost constant (in the four regions the $z = 1.5$ value is 96, 93, 77, 100 per cent the $z = 0$ value). Considering the shallower slope of the relation this result implies that the metal level was already built up in the core of the high- z clusters.

4.1.1 Evolution of the stellar fraction

In the previous section, we found a mild variation in the oxygen abundance only in the $[0.5 - 1]R_{500}$ radial range. We check, here, whether this is related to an increase of stellar content in that region. We, thus, consider how the stellar fraction, $f_*(< R) \equiv M_{star}(< R)/M_{tot}(< R)$, depends on the total mass, M_{500} , and how it evolves with time from $z = 1.5$ to $z = 0$. As found for the metal abundances and as expected, the stellar fraction exhibits negative gradient with radius: the stellar content is mostly concentrated in the central region ($r < 0.1R_{500}$) and rapidly decreases towards the outskirts (see also, e.g., Planelles et al. 2013; Battaglia et al. 2013). In the core $r < R_{500}$ there is a trend with the cluster mass but no significant evolution from $z = 1.5$ to $z = 0$. Precisely, the stellar fraction is 10-15 percent in the core of the smallest systems and about 4 – 5 percent in the largest clusters. The change of the relation normalisation, measured at $10^{14} M_{\odot}$, is less than 8 per cent. The result found in our simulations is in line with the recent observational study by Chiu et al. (2017), who also found an anti-correlation between stellar fraction and cluster mass within R_{500} (see also, Planelles et al. 2013) and no evidence of evolution in the redshift range between $z = 0.2$ and $z = 1.25$. However, if we restrict to the region $[0.5 - 1]R_{500}$ we do see that $10^{14} M_{\odot}$ clusters have a 30 per cent reduction in their stellar fraction (see Fig. 9). The amplitude of this variation is still small but, noticeably, goes

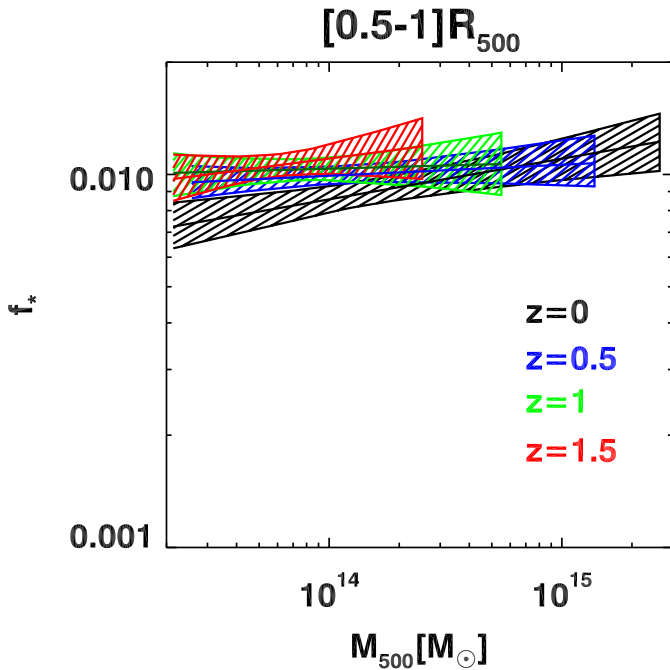


Figure 9. The stellar fraction-mass relation ($f_* - M_{500}$) in the AGN simulation shown at the radial range $[0.5 - 1]R_{500}$ for different redshifts. The solid lines represent the best-fit relations at those redshifts, while the line-filled areas specify the 68.3% confidence regions.

in the opposite direction with respect to the evolution of the oxygen abundance that we discuss in the previous section: while the abundance grows from $z=1.5$ to $z=0$, the stellar content decreases. The increase in metallicity therefore cannot be associated to fresh stellar formation, instead, it should be related to the accretion of already enriched gas, in addition to the accretion of pristine gas. In the next section, we investigate the role played by the AGN in raising the metal level in the outskirts of small groups.

4.2 The effects of AGN feedback on the mass-metallicity relation

Accounting that the iron and oxygen behaviours are very similar, in this Section we focus only on the former and we discuss the effect of the AGN on the mass-metallicity relation by comparing two sets of simulations obtained with and without the AGN.

In Fig. 10, we show how the iron abundance, Z_{Fe} , the hydrogen mass, M_H , the iron mass, M_{Fe} , and the stellar fraction vary with the total mass, M_{500} , in both simulations at $z = 0$. The four columns correspond to the different radial apertures from the core to the virial regions (from left to right). In the bottom panels, we enlighten the differences between the CSF and AGN results. The most striking difference on the abundance-mass relations derived in the two runs is that without AGN the relation cannot be represented by a single power-law rather there is a break at around $2 \times 10^{14} M_\odot$.

At the cluster scale ($M_{500} > 2 \times 10^{14} M_\odot$), the abundance dependence on mass shows the same trend in the two runs at all radii, but there is a clear off-set between the normalisations of the two relations. In the core, $r < 0.1R_{500}$, the CSF Z_{Fe} is about 60 percent higher than in the AGN run while in the two most external regions, $[0.5 - 1]R_{500}$ and $[1 - 2]R_{500}$, it is about 25 and 50 percent lower, respectively. To understand the origin of these ratios,

we look at the two separate contributions by the hydrogen mass and the iron mass in the second and third row, respectively. The gas fraction of the CSF clusters is always lower than that of the AGN clusters because the efficient radiative cooling, not regulated by the AGN activity, cools down a greater amount of hot gas that is subsequently converted in stars and thus is removed from the ICM. The phenomenon is in place at all radii but it is particularly strong in the core where the CSF runs host unrealistically massive bright central galaxies. The result of the excessive overall star formation is to drastically enhance the stellar fraction, as can be seen in the forth row. In the core and at fixed mass, CSF runs can have 3 times more stars than the AGN runs. In the CSF runs the star formation is actually still active at low-redshifts, however, the process does not lead to larger iron mass of the ICM with respect to the AGN clusters (third row), because the freshly formed metals are immediately locked back into newly formed stars. In this way the efficient stellar production of the CSF runs prevents the circulation of the metals from the star forming regions to the ICM. For this reason the iron mass is lower than the AGN outside the core. On the other hand, AGN feedback peaks at high redshift, when potential well of the (proto-)cluster is still relatively shallow and star formation is also quite intense. As consequence, this feedback channel plays a key role on spreading the metals created at high redshift. The process has the twofold effect of removing metals from star forming regions and of enriching the pristine gas that surrounded the small potential well of the early galaxies and that subsequently accrete into the low- z clusters (Biffi et al. 2017).

Both radiative cooling and AGN heating have a stronger impact in the lowest mass regime. The iron abundance in the CSF groups is largely reduced everywhere outside the core, while it agrees with the value in the AGN run in the innermost region. There, the hydrogen and iron masses depart from the AGN runs but with similar amplitude and sign. Indeed, generally the early activity of the AGN produces less concentrated groups with a reduced gas contribution. In addition to reducing the gas at disposal to produce new stars, the AGNs also heat the medium. Both phenomena quench star formation, thereby reducing the accretion of already enriched gas, so that iron abundance can only grow through the explosions of long-lived SNIa. Outside the core, the reduction in the gas mass in the CSF groups is comparable to that in the CSF clusters. However, the iron mass decreases even further in groups without AGN because the radiative cooling, which is more efficient in smaller systems, selectively removes highly enriched gas.

5 SUMMARY AND CONCLUSIONS

X-ray observations have shown that the intra-cluster gas metallicity appears to be distributed uniformly at large radii and exhibits no significant trend over cosmic time. We confirm these findings in our simulations (Biffi et al. 2017, 2018) and we investigate, here, how the ICM metallicity within a certain radial range depends on cluster scale expressed both as temperature and mass. The simulations are performed with an updated version of the GADGET-3 code which includes radiative cooling, star formation, metal enrichment, stellar and AGN feedback. Results from observational data are taken from Mantz et al. (2017) and from the CHEERS sample (de Plaa et al. 2017). The latter is analysed with the last updated atomic model for the metallicity estimation (Mernier et al., submitted). In the first part of our analysis, we compare our simulation results to these observational datasets and investigate how the ICM iron abundance varies as a function of the gas temperature. We particularly focus

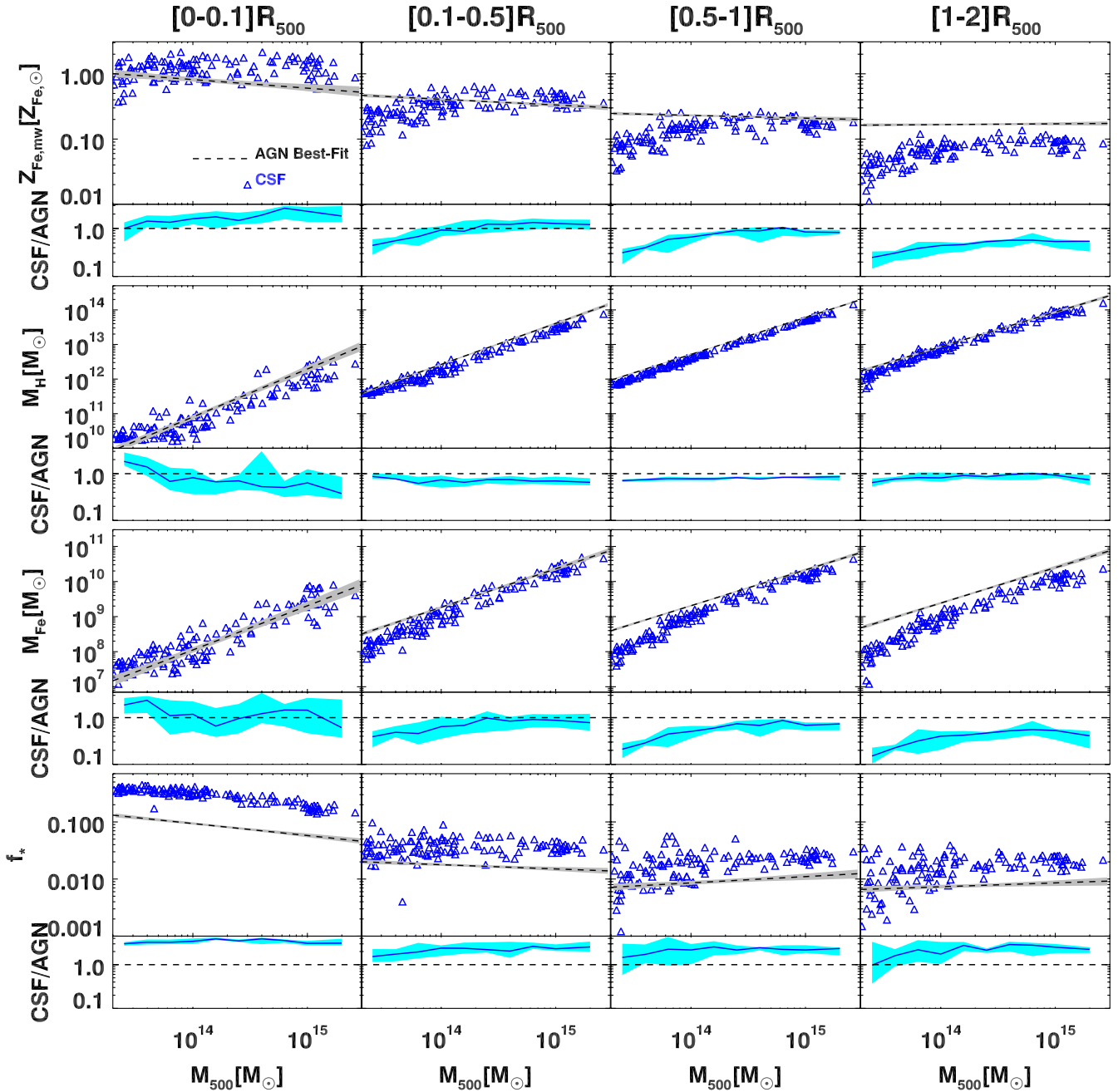


Figure 10. Comparison between AGN and CSF simulations at $z = 0$ for the relation between cluster total mass (M_{500}) and various quantities: iron abundance (Z_{Fe}), hydrogen mass (M_H), iron mass (M_{Fe}), and stellar mass fraction (f_*), for the four considered radial ranges. From top to bottom we show the $Z_{Fe} - M_{500}$, $M_H - M_{500}$, $M_{Fe} - M_{500}$, and $f_* - M_{500}$ relations, respectively. In the top sub-panels, the AGN results are represented by best-fit relations (dashed line) and the grey regions specify the 68.3% confidence regions. The bottom sub-panels show the median ratio (blue solid line) of the CSF value to the AGN best-fit relation as well as the 68.3% confidence region (cyan).

on potential biases, regarding the diversity of the core properties (CC and NCC) and selection effects, that might affect the observational analyses. In the second part, we carry out a study of the mass-metallicity relation for iron and oxygen and on its evolution. In addition, we also investigate how the mass-metallicity relation behaves when we remove the AGN feedback, in order to investigate its effect on the ICM metal enrichment. Throughout the study, we express both simulated and observed metallicity in terms of so-

lar metallicity as obtained from [Asplund et al. \(2009\)](#). The main results of our study can be summarised as follows:

- We compared the simulated $Z_{Fe} - T$ relation of the AGN simulations with the CHEERS sample which spans from groups to hot clusters. Both datasets show no evidence for a significant correlation between the ICM iron abundance and the ICM temperature measured in the core ($r < 0.1R_{500}$) of systems with $T_{[0-0.1]R_{500}} > 0.7$ keV. In particular, we did not find any significant break or feature that was present in earlier X-ray analysis.

When we split our simulated sample in CC and NCC clusters, the former subsample better agrees with the CHEERS data. In particular both simulated and observed cluster cores consistently show a mean value of Z_{Fe} of about $0.75 Z_{Fe,\odot}$ with a dispersion of 40% and 30%, respectively. Fitting the data with a power-law, we find a very shallow slope implying an extremely small variation in the abundances of groups and clusters (20-30 percent).

- When compared to the observed sample of massive clusters, with $T_{[0.1-0.5]R_{500}} > 5$ keV and $0 < z < 1.2$, from Mantz et al. (2017), the AGN simulations consistently reproduce the radial dependence of $Z_{Fe} - T$ relation for different radial ranges-dependence. For this sample of hot clusters, both simulated and observed data show a stronger correlation between iron abundance and temperature. However, we show with the whole simulated sample that the strong correlation of the $Z_{Fe} - T$ relation might be a bias induced by the selection of massive objects. Our simulations reveal no significant trend with redshift (with a variation lower than 20% since $z = 1$) in the $Z_{Fe} - T$ normalisation among all the considered radial ranges. This is at variance with respect to the results by Mantz et al. (2017), that present a stronger increase ($\sim 40\%$) of iron abundance at intermediate radii, $0.1R_{500} < r < 0.5R_{500}$. We notice, however, that among various observational works there is no agreement on the significance of this trend (see Ettori et al. 2015; McDonald et al. 2016).

- Both the iron and oxygen abundances of the AGN clusters exhibit an anti-correlation with cluster mass for regions within R_{500} , while no correlation is found in the cluster outskirts ($R_{500} < r < 2R_{500}$). However, fitting the relation with a power-law, we found that even in the core the slope is shallow ($\beta < -0.15$) implying that the metallicity is only few tens of percent different from poor groups to rich clusters. We do not detect any significant evolution for the relation since $z = 1.5$. Considering that the metallicity varies little across the mass scale and does not change in time, we can conclude that the majority of the iron and oxygen were already built up in the cluster core since high- z .

- The effect of the AGN feedback is studied by comparing the $Z_{Fe} - M_{500}$ relation obtained in runs performed with and without the AGN feedback. Without the AGN, the $z = 0$ systems present an higher stellar fraction at all radii but particularly in the core. The increase of the stellar fraction at each distance is almost independent on the mass of the system. The much higher stellar production, counter intuitively, is not associated to an increase of the iron mass of the ICM due to the fact that freshly produced metals are locked back into newly formed stars. Instead, the iron mass is comparable to the AGN case only in the core, but it is always reduced in the outskirts. This gap is scale-dependent being more extreme in the group scale, whereby causing the non-AGN iron abundance outside of the core dropped for systems with mass below $M_{500} \approx 2 \times 10^{14}$.

Our study shows that simulations and observations agree in supporting a weak variation of the ICM metallicity from groups to clusters of galaxies and that the metal content does not substantially varies with time. In addition, we confirm that when AGN feedback is included the level of metallicity in the outskirts is flat and at a rather high level (about 20-30 percent of the solar value). All these findings further support the early enrichment scenario.

However, there is still ample space for future works from both simulation and observation sides to consolidate the results. Future observations will be needed to improve the current statistics in the group regime. With the current X-ray telescopes, it is challenging to increase the number of observed small systems (e.g., those with temperature below 1 keV) as they are extremely faint in the X-

ray band. In this regard, the next generation of X-ray telescopes, such as *ATHENA*⁴, would be of extremely utility in observing low-mass systems (Nandra et al. 2013; Pointecouteau et al. 2013). The *ATHENA* telescope, with large effective area and high-resolution spectroscopy, is expected to provide robust estimation of the gas-phase metallicity in the group regime.

From the numerical point of view, it is worth noting that currently the diffusion of metals is implemented by spreading the metals to gas particles within the kernel but the code does not foresee an accurate metal diffusion model. In addition, we have not included dust formation and destruction which should be considered for an accurate description of the metal content. Also, the current model of AGN feedback is exclusively thermal, while the mechanical AGN feedback (e.g., jets and outflow) is relevant for anisotropically ejecting metals at larger radii from the core.

ACKNOWLEDGEMENTS

This work was supported by the Lendület LP2016-11 grant awarded by the Hungarian Academy of Sciences. We acknowledge financial support from the agreement ASI-INAF n.2017-14-H.0, the INFN INDARK grant, and Consorzio per la Fisica of Trieste. M.G. is supported by NASA through Einstein Postdoctoral Fellowship Award Number PF5-160137 issued by the Chandra X-ray Observatory Center, which is operated by the SAO for and on behalf of NASA under contract NAS8-03060. Support for this work was also provided by Chandra grant GO7-18121X. SP is “Juan de la Cierva” fellow (ref. IJCI-2015-26656) of the Spanish Ministerio de Economía y Competitividad (MINECO) and acknowledges additional support from the MINECO through the grant AYA2016-77237-C3-3-P and the Generalitat Valenciana (grant GVACOMP2015-227). DF acknowledges financial support from the Slovenian Research Agency (research core funding No. P1-0188).

REFERENCES

- Asplund M., Grevesse N., Sauval A.J., Scott P., 2009, *ARA&A*, 47, 481
 Barnes D.J., et al., 2017, *MNRAS*, 471, 1088
 Battaglia N., Bond J.R., Pfrommer C., Sievers J.L., 2013, *ApJ*, 777, 123
 Beck A.M., et al., 2016, *MNRAS*, 455, 2110
 Biffi V., Planelles S., Borgani S., Rasia E., Murante G., Fabjan D., Gaspari M., 2018, *MNRAS*
 Biffi V., et al., 2016, *ApJ*, 827, 112
 Biffi V., et al., 2017, *MNRAS*, 468, 531
 Böhringer H., Werner N., 2010, *A&A Rev.*, 18, 127
 Bonafede A., Dolag K., Staszyszyn F., Murante G., Borgani S., 2011, *MNRAS*, 418, 2234
 Borgani S., Fabjan D., Tornatore L., Schindler S., Dolag K., Diaferio A., 2008, *Space Sci. Rev.*, 134, 379
 Chabrier G., 2003, *Publ. Astr. Soc. Pac.*, 115, 763
 Chiu I., et al., 2017, *ArXiv e-prints*
 De Grandi S., Ettori S., Longhetti M., Molendi S., 2004, *A&A*, 419, 7
 de Plaa J., et al., 2017, *A&A*, 607, A98
 Ettori S., Gastaldello F., Gitti M., O’Sullivan E., Gaspari M., Brighenti F., David L., Edge A.C., 2013, *A&A*, 555, A93
 Ettori S., Baldi A., Balestra I., Gastaldello F., Molendi S., Tozzi P., 2015, *A&A*, 578, A46
 Frenk C.S., et al., 1999, *ApJ*, 525, 554

⁴ <http://www.the-athena-x-ray-observatory.eu/>

Table 1. Best-fitting parameters of the $Z_{Fe} - T$ relation in the clusters core ($[0 - 0.1]R_{500}$), as described by Eq. (4), for different AGN simulated samples shown along with the observational CHEERS sample. Also reported the Spearman's rank correlation coefficients (r_s) and the significance of their deviation (in parentheses) from zero given the null-hypothesis.

Sample	$\log_{10}(Z_{0T} [Z_{Fe,\odot}])$	β_T	$\sigma \log_{10} Z_{Fe} T$	r_s
AGN full	-0.178 ± 0.011	-0.10 ± 0.04	0.16 ± 0.01	$-0.21 (2 \times 10^{-3})$
AGN NCC	-0.190 ± 0.013	-0.14 ± 0.04	0.16 ± 0.01	$-0.27 (4 \times 10^{-4})$
AGN CC	-0.157 ± 0.023	0.01 ± 0.07	0.15 ± 0.02	$-0.08 (6 \times 10^{-1})$
CHEERS data	-0.127 ± 0.019	0.00 ± 0.06	0.11 ± 0.01	$+0.05 (8 \times 10^{-1})$

Table 2. Best-fitting parameters of the relation in Eq. (6) for the AGN simulation shown along with the results from Mantz et al. 2017. The Spearman's rank correlation coefficients (r_s) for the AGN simulation and the significance of their deviation from zero (in parentheses) are also reported (these quantities are not available, N/A, for the observational data).

Aperture	z_{piv}	$T_{\text{piv}}[\text{keV}]$	$\log_{10}(Z_{0T} [Z_{Fe,\odot}])$	β_T	γ_z	$\sigma_{\log_{10} Z_{Fe} T}$	r_s
AGN							
$[0.0 - 0.1]R_{500}$	0.23	6.4	-0.230 ± 0.011	-0.38 ± 0.11	-0.32 ± 0.13	0.09 ± 0.01	$-0.40 (4 \times 10^{-4})$
$[0.1 - 0.5]R_{500}$	0.19	8.0	-0.440 ± 0.009	-0.05 ± 0.08	-0.18 ± 0.06	0.045 ± 0.004	$+0.01 (9 \times 10^{-1})$
$[0.5 - 1]R_{500}$	0.17	6.7	-0.720 ± 0.016	-0.47 ± 0.09	-0.34 ± 0.10	0.07 ± 0.01	$-0.38 (9 \times 10^{-4})$
Mantz et al. (2017)							
$[0.0 - 0.1]R_{500}$	0.23	6.4	-0.217 ± 0.009	-0.35 ± 0.06	-0.14 ± 0.17	0.08 ± 0.01	N/A
$[0.1 - 0.5]R_{500}$	0.19	8.0	-0.384 ± 0.007	0.10 ± 0.07	-0.71 ± 0.15	0.04 ± 0.01	N/A
$[0.5 - 1]R_{500}$	0.17	6.7	-0.622 ± 0.040	0.22 ± 0.34	-0.30 ± 0.91	$0.00^{+0.07}_{-0.00}$	N/A

Table 3. Best-fitting parameters of Eq. (7) for the $Z_{Fe} - M_{500}$ and $Z_O - M_{500}$ relations in the AGN simulation, shown along with Spearman's correlation coefficients and the significance (in the parentheses) of their deviation from zero given the null-hypothesis.

AGN	Fe				O			
z	$\log_{10}(Z_{0,Fe} [Z_{\odot}])$	β_{Fe}	$\sigma_{\log_{10} Z_{Fe} M}$	$r_{s,Fe}$	$\log_{10}(Z_{0,O} [Z_{\odot}])$	β_O	$\sigma_{\log_{10} Z_O M}$	$r_{s,O}$
$[0.0 - 0.1]R_{500}$								
0.0	-0.088 ± 0.015	-0.131 ± 0.025	0.141 ± 0.010	$-0.49 (1 \times 10^{-7})$	-0.183 ± 0.018	-0.101 ± 0.028	0.163 ± 0.012	$-0.39 (3 \times 10^{-5})$
0.5	-0.143 ± 0.011	-0.116 ± 0.028	0.139 ± 0.008	$-0.30 (2 \times 10^{-4})$	-0.189 ± 0.013	-0.124 ± 0.031	0.161 ± 0.009	$-0.30 (2 \times 10^{-4})$
1.0	-0.158 ± 0.011	-0.111 ± 0.032	0.120 ± 0.007	$-0.29 (6 \times 10^{-4})$	-0.200 ± 0.014	-0.111 ± 0.041	0.149 ± 0.009	$-0.19 (3 \times 10^{-2})$
1.5	-0.175 ± 0.014	-0.099 ± 0.042	0.103 ± 0.008	$-0.28 (5 \times 10^{-3})$	-0.196 ± 0.018	-0.118 ± 0.056	0.138 ± 0.011	$-0.24 (2 \times 10^{-2})$
$[0.1 - 0.5]R_{500}$								
0.0	-0.390 ± 0.007	-0.090 ± 0.012	0.067 ± 0.005	$-0.60 (2 \times 10^{-11})$	-0.512 ± 0.008	-0.092 ± 0.013	0.075 ± 0.005	$-0.56 (7 \times 10^{-10})$
0.5	-0.424 ± 0.006	-0.110 ± 0.016	0.078 ± 0.004	$-0.50 (1 \times 10^{-11})$	-0.533 ± 0.007	-0.120 ± 0.017	0.085 ± 0.005	$-0.51 (1 \times 10^{-11})$
1.0	-0.447 ± 0.006	-0.112 ± 0.018	0.067 ± 0.004	$-0.42 (3 \times 10^{-7})$	-0.547 ± 0.007	-0.114 ± 0.020	0.073 ± 0.005	$-0.41 (8 \times 10^{-7})$
1.5	-0.478 ± 0.009	-0.107 ± 0.026	0.067 ± 0.005	$-0.37 (2 \times 10^{-4})$	-0.564 ± 0.011	-0.117 ± 0.033	0.082 ± 0.006	$-0.31 (2 \times 10^{-3})$
$[0.5 - 1.0]R_{500}$								
0.0	-0.637 ± 0.007	-0.045 ± 0.011	0.063 ± 0.004	$-0.37 (1 \times 10^{-4})$	-0.780 ± 0.008	-0.048 ± 0.012	0.073 ± 0.005	$-0.37 (1 \times 10^{-4})$
0.5	-0.676 ± 0.005	-0.058 ± 0.013	0.066 ± 0.004	$-0.35 (6 \times 10^{-6})$	-0.816 ± 0.006	-0.080 ± 0.015	0.072 ± 0.004	$-0.40 (1 \times 10^{-7})$
1.0	-0.711 ± 0.006	-0.075 ± 0.017	0.064 ± 0.004	$-0.34 (4 \times 10^{-5})$	-0.852 ± 0.007	-0.094 ± 0.019	0.072 ± 0.004	$-0.40 (1 \times 10^{-6})$
1.5	-0.749 ± 0.008	-0.095 ± 0.024	0.058 ± 0.004	$-0.37 (2 \times 10^{-4})$	-0.889 ± 0.009	-0.106 ± 0.028	0.065 ± 0.005	$-0.39 (6 \times 10^{-5})$
$[1.0 - 2.0]R_{500}$								
0.0	-0.778 ± 0.006	0.012 ± 0.011	0.059 ± 0.004	$+0.09 (4 \times 10^{-1})$	-0.921 ± 0.007	0.008 ± 0.011	0.065 ± 0.005	$+0.07 (5 \times 10^{-1})$
0.5	-0.782 ± 0.005	0.012 ± 0.012	0.060 ± 0.003	$+0.05 (5 \times 10^{-1})$	-0.930 ± 0.005	0.011 ± 0.013	0.065 ± 0.004	$+0.04 (7 \times 10^{-1})$
1.0	-0.781 ± 0.006	-0.052 ± 0.018	0.066 ± 0.004	$-0.20 (2 \times 10^{-2})$	-0.928 ± 0.007	-0.040 ± 0.021	0.074 ± 0.004	$-0.14 (1 \times 10^{-1})$
1.5	-0.805 ± 0.009	-0.085 ± 0.025	0.065 ± 0.005	$-0.27 (7 \times 10^{-3})$	-0.937 ± 0.009	-0.067 ± 0.027	0.066 ± 0.005	$-0.21 (3 \times 10^{-2})$

Table 4. Best-fitting parameters of the relation in Eq. (8) for the normalisation evolution of the $Z_{Fe} - M_{500}$ and $Z_O - M_{500}$ relations in the AGN simulation.

Radial Range	Fe		O	
	$\log_{10} A_{Fe}$	B_{Fe}	$\log_{10} A_O$	B_O
$[0.0 - 0.1]R_{500}$	-0.090 ± 0.016	-0.22 ± 0.03	-0.175 ± 0.003	-0.05 ± 0.01
$[0.1 - 0.5]R_{500}$	-0.404 ± 0.012	-0.18 ± 0.02	-0.528 ± 0.008	-0.08 ± 0.02
$[0.5 - 1.0]R_{500}$	-0.623 ± 0.008	-0.29 ± 0.02	-0.762 ± 0.006	-0.29 ± 0.01
$[1.0 - 2.0]R_{500}$	-0.765 ± 0.007	-0.06 ± 0.02	-0.911 ± 0.007	-0.05 ± 0.01

- Gaspari M., Brighenti F., Ruszkowski M., 2013, *Astronomische Nachrichten*, 334, 394
- Gaspari M., et al., 2018, *ApJ*, 854, 167
- Haardt F., Madau P., 2001, in D.M. Neumann, J.T.V. Tran, eds., *Clusters of Galaxies and the High Redshift Universe Observed in X-rays*, p. 64
- Hitomi Collaboration, et al., 2017, *Nature*, 551, 478
- Karakas A.I., 2010, *MNRAS*, 403, 1413
- Kelly B.C., 2007, *ApJ*, 665, 1489
- Kirkpatrick C.C., McNamara B.R., Cavagnolo K.W., 2011, *ApJL*, 731, L23
- Leccardi A., Rossetti M., Molendi S., 2010, *A&A*, 510, A82
- Mantz A.B., Allen S.W., Morris R.G., Simionescu A., Urban O., Werner N., Zhuravleva I., 2017, *ArXiv e-prints*
- Mazzotta P., Rasia E., Moscardini L., Tormen G., 2004, *MNRAS*, 354, 10
- McDonald M., et al., 2016, *ApJ*, 826, 124
- Mernier F., de Plaa J., Pinto C., Kaastra J.S., Kosec P., Zhang Y.Y., Mao J., Werner N., 2016, *A&A*, 592, A157
- Nandra K., et al., 2013, *ArXiv e-prints*
- Padovani P., Matteucci F., 1993, *ApJ*, 416, 26
- Planelles S., Borgani S., Dolag K., Ettori S., Fabjan D., Murante G., Tornatore L., 2013, *MNRAS*, 431, 1487
- Planelles S., et al., 2017, *MNRAS*, 467, 3827
- Pointecouteau E., et al., 2013, *ArXiv e-prints*
- Rasia E., et al., 2015, *ApJL*, 813, L17
- Romano D., Karakas A.I., Tosi M., Matteucci F., 2010, *A&A*, 522, A32
- Schindler S., Diaferio A., 2008, *Space Sci. Rev.*, 134, 363
- Smith R.K., Brickhouse N.S., Liedahl D.A., Raymond J.C., 2001, *ApJL*, 556, L91
- Springel V., 2005, *MNRAS*, 364, 1105
- Springel V., Hernquist L., 2003, *MNRAS*, 339, 289
- Springel V., Di Matteo T., Hernquist L., 2005, *MNRAS*, 361, 776
- Steinborn L.K., Dolag K., Hirschmann M., Prieto M.A., Remus R.S., 2015, *MNRAS*, 448, 1504
- Sun M., 2012, *New Journal of Physics*, 14, 045004
- Thielemann F.K., et al., 2003, in W. Hillebrandt, B. Leibundgut, eds., *From Twilight to Highlight: The Physics of Supernovae*, p. 331
- Tornatore L., Borgani S., Dolag K., Matteucci F., 2007, *MNRAS*, 382, 1050
- Truong N., et al., 2018, *MNRAS*, 474, 4089
- Urban O., Werner N., Allen S.W., Simionescu A., Mantz A., 2017, *MNRAS*, 470, 4583
- Villaescusa-Navarro F., et al., 2016, *MNRAS*, 456, 3553
- Vogelsberger M., et al., 2017, *ArXiv e-prints*
- Werner N., Durret F., Ohashi T., Schindler S., Wiersma R.P.C., 2008, *Space Sci. Rev.*, 134, 337
- Werner N., Urban O., Simionescu A., Allen S.W., 2013, *Nature*, 502, 656
- White S.D.M., Navarro J.F., Evrard A.E., Frenk C.S., 1993, *Nature*, 366, 429
- Wiersma R.P.C., Schaye J., Smith B.D., 2009, *MNRAS*, 393, 99
- Woosley S.E., Weaver T.A., 1995, *ApJS*, 101, 181
- Yates R.M., Thomas P.A., Henriques B.M.B., 2017, *MNRAS*, 464, 3169